

Shaoping Lu¹, Faqi Liu¹, Nizar Chemingui¹, Alejandro Valenciano¹, and Andrew Long¹

Abstract

We present a least-squares solution for depth migration of the full reflected wavefield. The algorithm combines primary and high-order reflected energy and significantly enhances the image illumination and resolution compared to those of conventional migration. Least-squares full-wavefield migration (LS-FWM) directly computes the earth's reflectivity, thereby avoiding crosstalk noise often observed in imaging using high-order reflections. Iteratively solving an inversion problem is computationally intensive and can suffer from instability issues; however, we develop an efficient least-squares procedure by combining a fast and accurate one-way wave-equation propagator with an effective linear inversion solver. An advanced regularization method is also employed to stabilize the inversion by controlling the over-fitting problem. Successful applications to both synthetic and field data examples demonstrate that LS-FWM greatly improves the imaging illumination and resolution compared to conventional migration.

Introduction

Linear inversion applications to seismic imaging are well established (e.g., Schuster, 1993; Nemeth et al., 1999; Prucha and Biondi, 2002; Valenciano et al., 2006). We implicitly implement least-squares migration (LSM) by means of data domain residual reduction in an iterative fashion, using a viscoacoustic anisotropic one-way wave-equation propagator that can utilize modern broadband seismic content and the high-resolution velocity information available from full-waveform inversion (FWI) (Lailly, 1983; Tarantola, 1984). A fast inversion solver with an advanced regularization scheme also ensures a stable implementation.

Standard band-limited depth migration of primary reflections often yields insufficient imaging illumination and resolution that can be attributed to limitations in both the acquisition geometry and processing technology employed. Recent efforts to improve imaging resolution have promoted new acquisition strategies that generate data with broader bandwidth (e.g., Carlson et al., 2007). Furthermore, FWI can facilitate high-definition earth models that enable high-resolution depth imaging. Wavefield distortions associated with complex geology and limitations in the acquisition geometry remain unresolved; however, the least-squares method poses depth migration as an inversion problem that significantly improves the amplitude fidelity and resolution of depth images.

Separated-wavefield imaging (SWIM) uses the downgoing pressure wavefield to exploit the extended illumination provided by surface-multiple energy, effectively converting all receivers into virtual sources (Lu et al., 2015). Standard migration of primaries and SWIM are complementary and can augment the overall imaging results when they are combined correctly. While full-wavefield migration (FWM) is able to jointly image both primary and high-order reflected energy, it cannot easily balance the contribution of each component (primary imaging and

SWIM). Furthermore, FWM also involves crosstalk due to the natural blending scheme. Although certain processes such as deconvolution imaging condition or crosstalk prediction can be applied to attenuate crosstalk (Lu et al., 2016), none fundamentally resolves the problem. In contrast, our least-squares full-wavefield migration (LS-FWM) solution directly computes the earth reflectivity, balances the contributions of primary and multiple energy, and produces an image that is free of crosstalk interference noise.

Least-squares migration

Given the observed data d_{obs} , seismic imaging finds the earth reflectivity m . Standard depth migration produces an approximation to the earth's reflectivity m

$$m = L^* d_{obs}, \quad (1)$$

where operator L^* is the adjoint (conjugate transpose) of the modeling operator L . Standard migration is able to produce a structural image of the earth; however, this result often displays uneven illumination, narrow bandwidth, and limited wavenumber content, because the migration is not the inverse of a modeling operation.

Different from conventional migration (equation 1), LSM resolves the inverse of the modeling process

$$m = (LL)^{-1} L^* d_{obs}, \quad (2)$$

by solving a minimization problem

$$m = \arg \min \frac{1}{2} \| d_{obs} - Lm \|^2. \quad (3)$$

The solution in equation 2 can be obtained using two distinct methods. The first method explicitly computes the matrix L^*L and its inverse, or alternatively, an implicit method can be used here iteratively to invert the operator L .

Iterative LSM. The iterative LSM algorithm described here is summarized in Figure 1, which is implemented in a migration/demigration framework. One inversion iteration (loop) consists

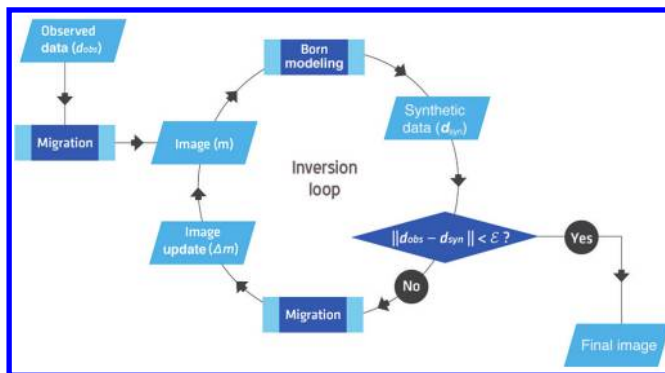


Figure 1. An iterative LSM algorithm.

¹PGS.

<https://doi.org/10.1190/tle37010046.1>

of one Born modeling (Cohen et al., 1986) and one migration. The first step of LSM is a standard migration, following which the migrated image is used as a reflectivity model in Born modeling. When the mismatch between the simulated and observed data is large, the data residual $d_{obs} - d_{syn}$ will be migrated and used to update the image m . The inversion converges when the mismatch is within an acceptable threshold.

Adjoint operators and fast linear inversion solvers. A migration operator (L^*) is the conjugate transpose of a modeling operator. In general, the full-modeling operator matrix L is too big to fit in the memory of a computing system, so it is not convenient to formulate the L matrix and compute its adjoint L^* explicitly. Instead of saving the full matrices, we implicitly formulate the modeling operator L and its adjoint L^* , and then use the dot product test (equation 4) to ensure the adjoint property of the demigration L and migration L^* operators

$$\langle Lm, d \rangle = \langle m, L^*d \rangle, \quad (\forall m, d). \quad (4)$$

The operator L and its adjoint L^* pass the dot product test when equation 4 is satisfied for any matrix m and d .

The availability of the adjoint operator pair L and L^* enables the use of a fast linear inversion solver such as LSQR (Paige and Saunders, 1982) in the LSM. Among many different algorithms, Lanczos Bidiagonalization-based LSQR calculates the least-squares solution for m by recursively applying matrix-vector and vector-vector products. LSQR is highly efficient

and stable as there is neither matrix inversion nor matrix decomposition required.

Regularization and randomized Kaczmarz algorithm. LSM is traditionally ill posed due to the band-limited nature of seismic data and the limitations of the acquisition geometries. Therefore, specific regularization effort is required to guide the minimization procedure to avoid over-fitting issues such as the “ringiness” in the inversion result (Figure 2a), or nonphysical migration swings caused by limited acquisition aperture (Figure 2c). To stabilize the inversion and control the over-fitting problem, an L_1 steering variation (SV) regularization is used in our inversion algorithm (Qiu et al., 2016), which is a projection constraint based upon the L_1 total variation (TV) algorithm (Rudin et al., 1992; Goldstein and Osher, 2009),

$$m = \arg \min \left[\frac{1}{2} \|d_{obs} - Lm\|_2^2 + \|\lambda_x \partial_x m\|_{L_1} + \|\lambda_y \partial_y m\|_{L_1} + \|\lambda_z \partial_z m\|_{L_1} \right]. \quad (5)$$

The L_1 norms in equation 5 pursue a sparse representation of the reflectivity m , which is one of the most important objectives of LSM. While regularization can dampen the inversion and slow down the convergence, we implement the SV regularization using the randomized Kaczmarz algorithm (Strohmer and Vershynin, 2009), which allows us to use only a subset of the observation in each iteration to improve computation efficiency.

Inversion solution for FWM. Inversion solutions for conventional primary migration and FWM are facilitated via different boundary data as summarized in Table 1. In LSM of primaries, an impulse source is used as the boundary condition for the modeling operator L , and the upgoing primary wavefield P_{up} (primaries) as boundary observation d_{obs} for inversion. LS-FWM uses the downgoing wavefield P_{down} plus an impulse source as the boundary condition for the modeling operator L and the total upgoing wavefield P_{up} (total) consisting of both primaries and multiples as boundary observation d_{obs} for inversion.

Table 1. A comparison of least-squares solutions for migration of primaries (LSM) and FWM (LS-FWM). LSM and LS-FWM share the same computation engine with different boundary conditions. LSM of primaries uses an impulse source wavefield as the boundary condition for the modeling operator L and the upgoing primaries P_{up} (primaries) as boundary observation d_{obs} for inversion. LS-FWM uses the downgoing wavefield P_{down} plus an impulse source as the boundary condition for the modeling operator L and the total upgoing wavefield P_{up} (total) consisting of both primaries and multiples as boundary observation d_{obs} for inversion.

	Boundary source wavefield (boundary condition for L)	Boundary receiver wavefield (boundary observation d_{obs})
LSM	impulsive source	P_{up} (primaries)
LS-FWM	impulsive source + P_{down}	P_{up} (total)

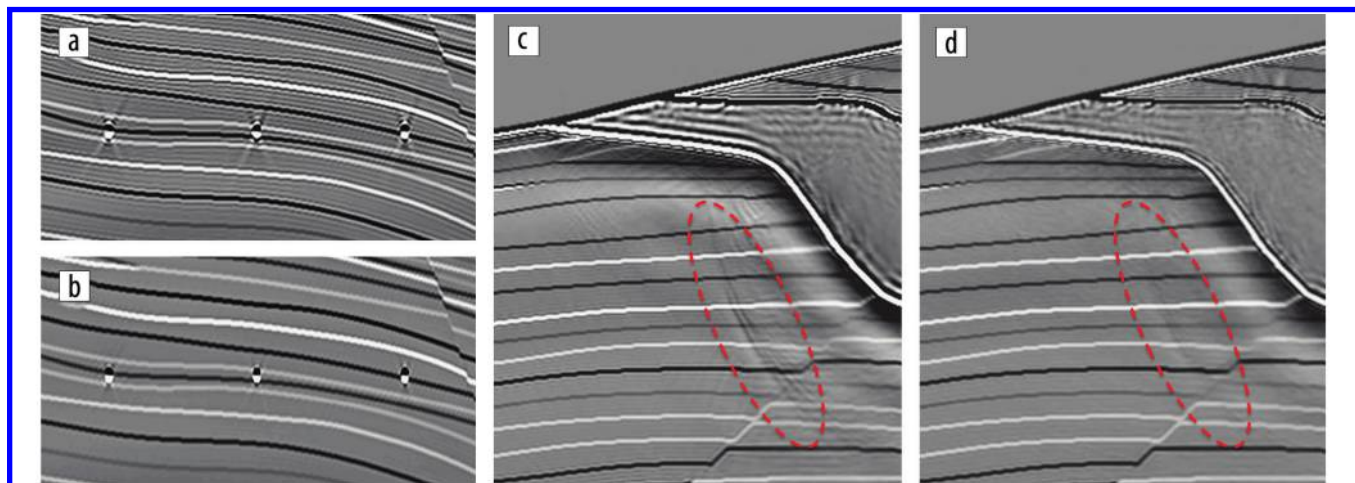


Figure 2. LSM results: (a) and (c) without SV regularization, and (b) and (d) with SV regularization. Regularization stabilizes LSM by correcting overfitting issues such as the ringiness in (a) and the migration noise in (c), which is indicated by the red ovals.

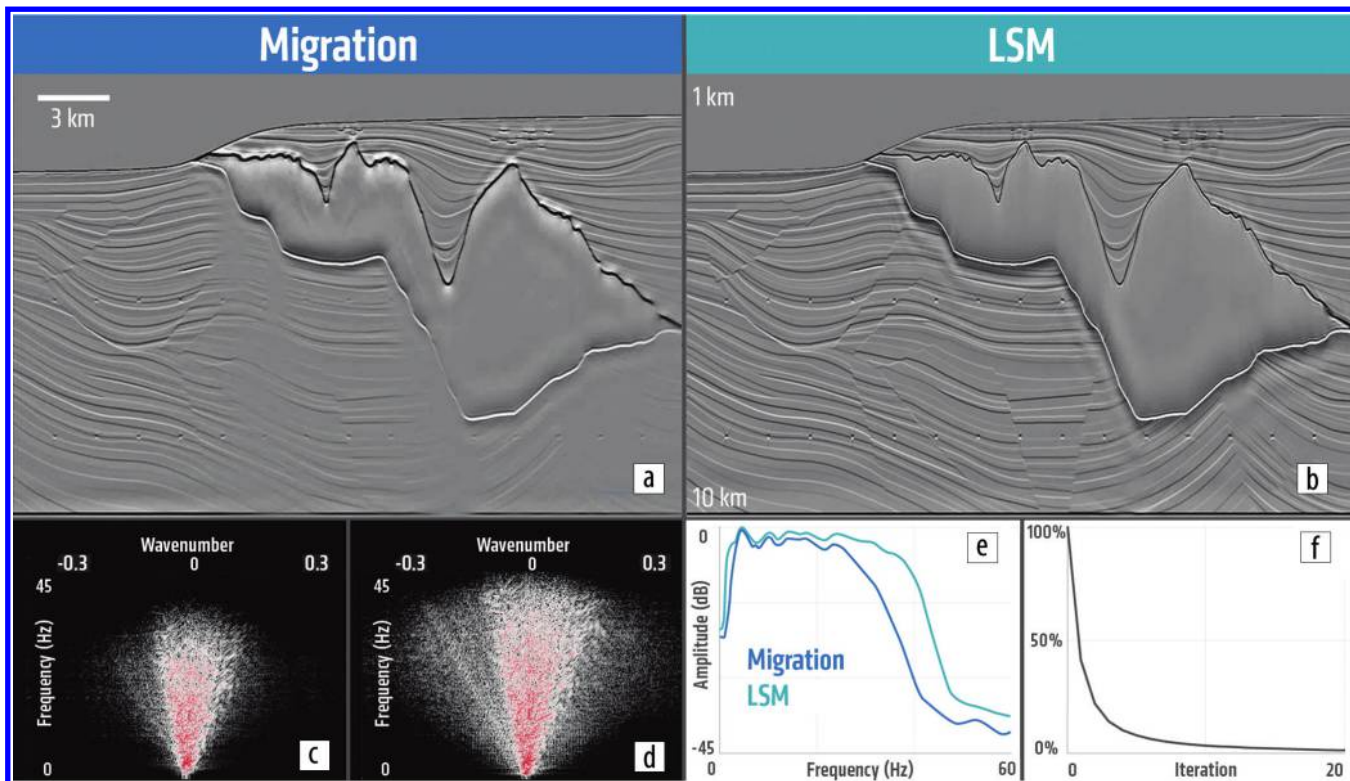


Figure 3. Sigsbee2b 2D synthetic example: (a) migration image; (b) LSM image; (c) $f-k$ spectrum of migration image; (d) $f-k$ spectrum of LSM image; (e) frequency spectra of migration (blue) and LSM (teal); and (f) normalized LSM objective function convergence rate.

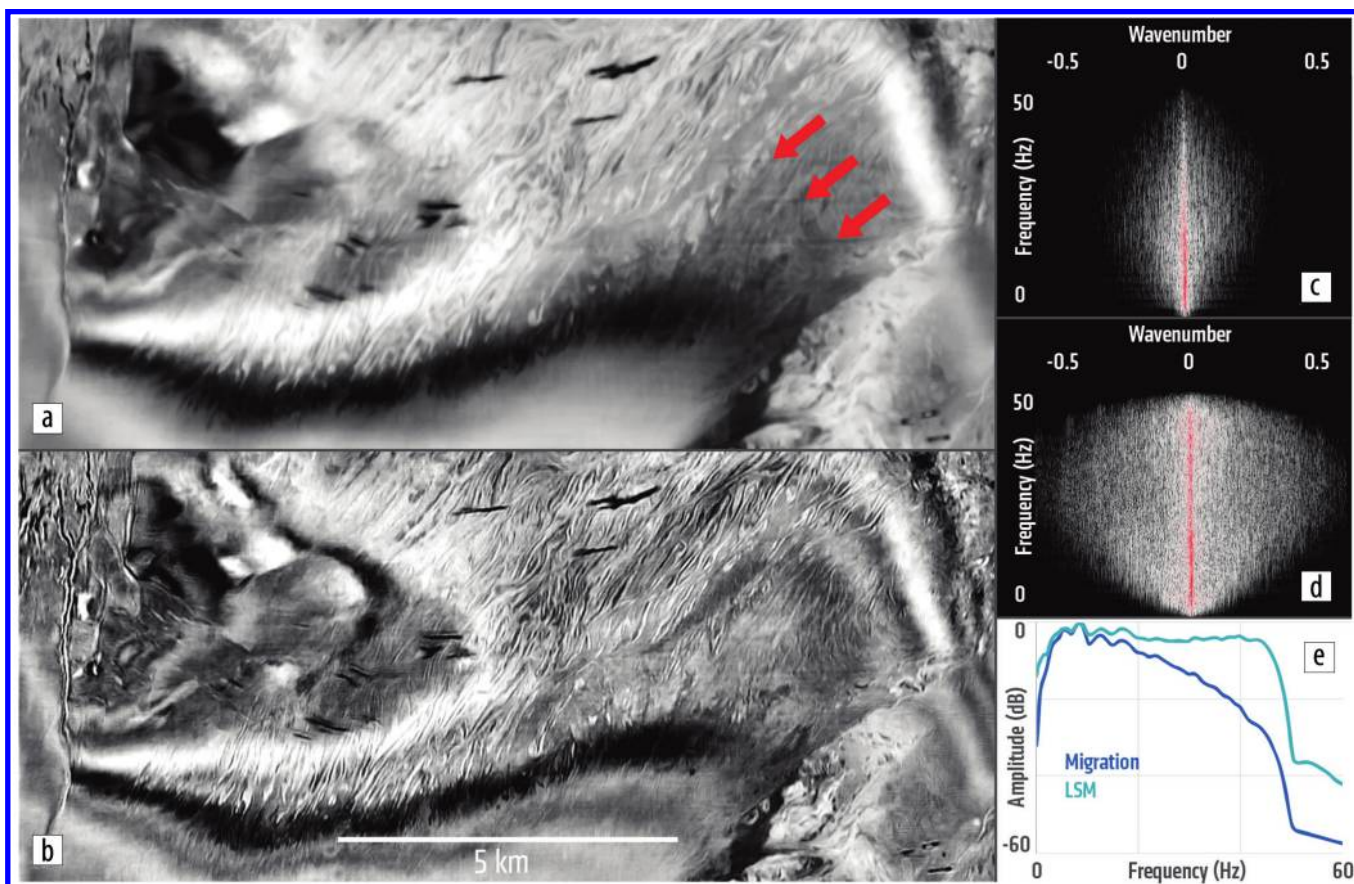


Figure 4. Gulf 3D WAZ field data example: (a) depth slice at 1150 m from migration (red arrows indicate acquisition footprints); (b) depth slice at 1150 m from LSM; (c) migration $f-k$ spectrum; (d) LSM $f-k$ spectrum; and (e) frequency spectra of migration and LSM.

consisting of both primaries and multiples, acts as boundary observation d_{obs} for inversion.

Since FWM images both primary and multiple reflected energy simultaneously, it can produce improved images in comparison to standard migration of primaries only. However, it is challenging to balance the primary and multiple

components obtained from using a plain migration. In addition, the FWM results are contaminated by crosstalk noise created by the interference terms in the encoded migration algorithm. Conversely, the least-squares solution resolves an inverse problem that excludes the cross terms (equation 2). LS-FWM computes a reflectivity image that explains the observed data

without involving the interference noise and automatically balances the energy from each component.

Synthetic and field data examples

Least-squares migration of primaries. We applied LSM to the 2D Sigsbee2b synthetic data. The depth images are displayed in Figure 3. The standard migration result in Figure 3a shows uneven illumination throughout the sedimentary and subsalt areas, including shadow zones related to the complex salt morphology. LSM improves the illumination by balancing the amplitudes and reducing the effects of the shadow zones in Figure 3b, and so enhances the temporal resolution by broadening the frequency spectrum (Figure 3e). Figures 3c and 3d also show that LSM balances the wavenumber content, which improves the imaging of the faults and dipping salt flanks. Furthermore, LSM converges rapidly, reducing the data residuals by 90% in only four iterations (Figure 3f).

We also applied LSM to wide-azimuth (WAZ) data from the Gulf of Mexico. The depth images in Figures 4 and 5 demonstrate that LSM can deliver superior images compared to standard migration. The image improvements of LSM over the standard migration include a reduction of acquisition footprint (indicated by arrows), much higher temporal and spatial resolution, and improved wavenumber content (Figures 4c–4e). In Figure 5, the inline and crossline images from LSM (Figures 5c and 5d) reveal significant spatial-resolution improvement by better resolving the fault structures. Also, LSM enhances illumination of the deeper section and creates an image with balanced amplitude.

The results in Figure 6 are from a 3D narrow-azimuth (NAZ) data set from the North Sea. They illustrate the advantages of applying LSM in the presence of strong attenuation using a high-resolution velocity model

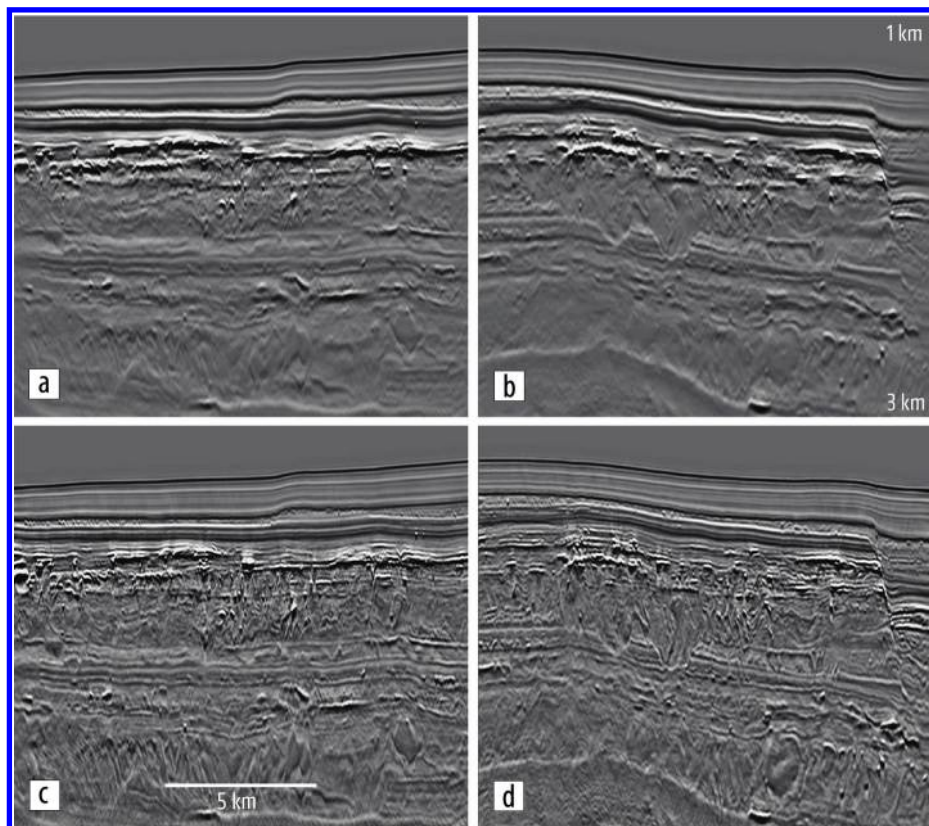


Figure 5. Gulf 3D WAZ field data examples: (a) migration inline image; (b) migration crossline image; (c) LSM inline image; and (d) LSM crossline image.

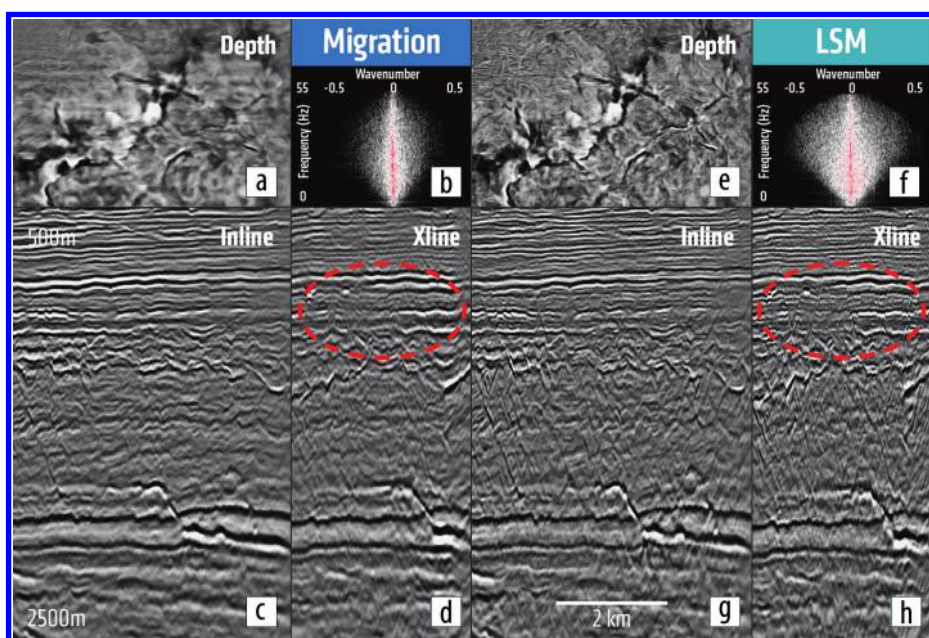


Figure 6. A 3D NAZ field data example from the North Sea. Left: migration results. Right: LSM results. The depth slice is at 1.8 km (top reservoir). The fault planes are much better imaged by LSM (indicated by the red ovals).

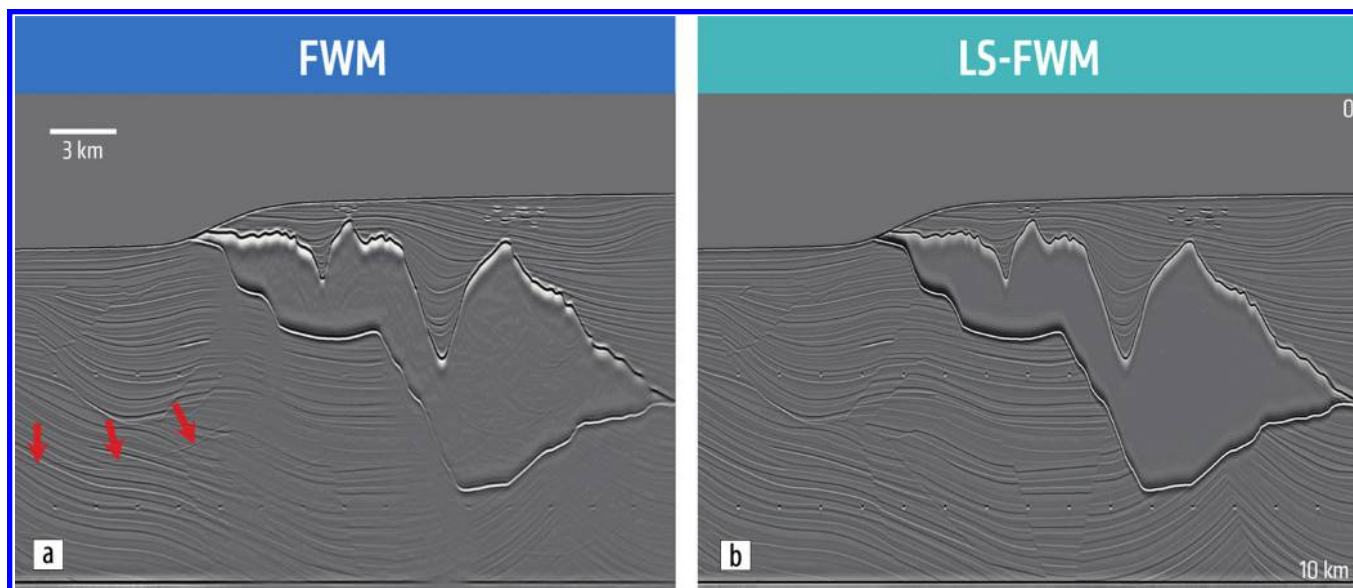


Figure 7. (a) FWM versus (b) LS-FWM with synthetic 2D Sigsbee2b data. FWM involves crosstalk which is indicated by red arrows in (a) and LS-FWM successfully mitigates the crosstalk.

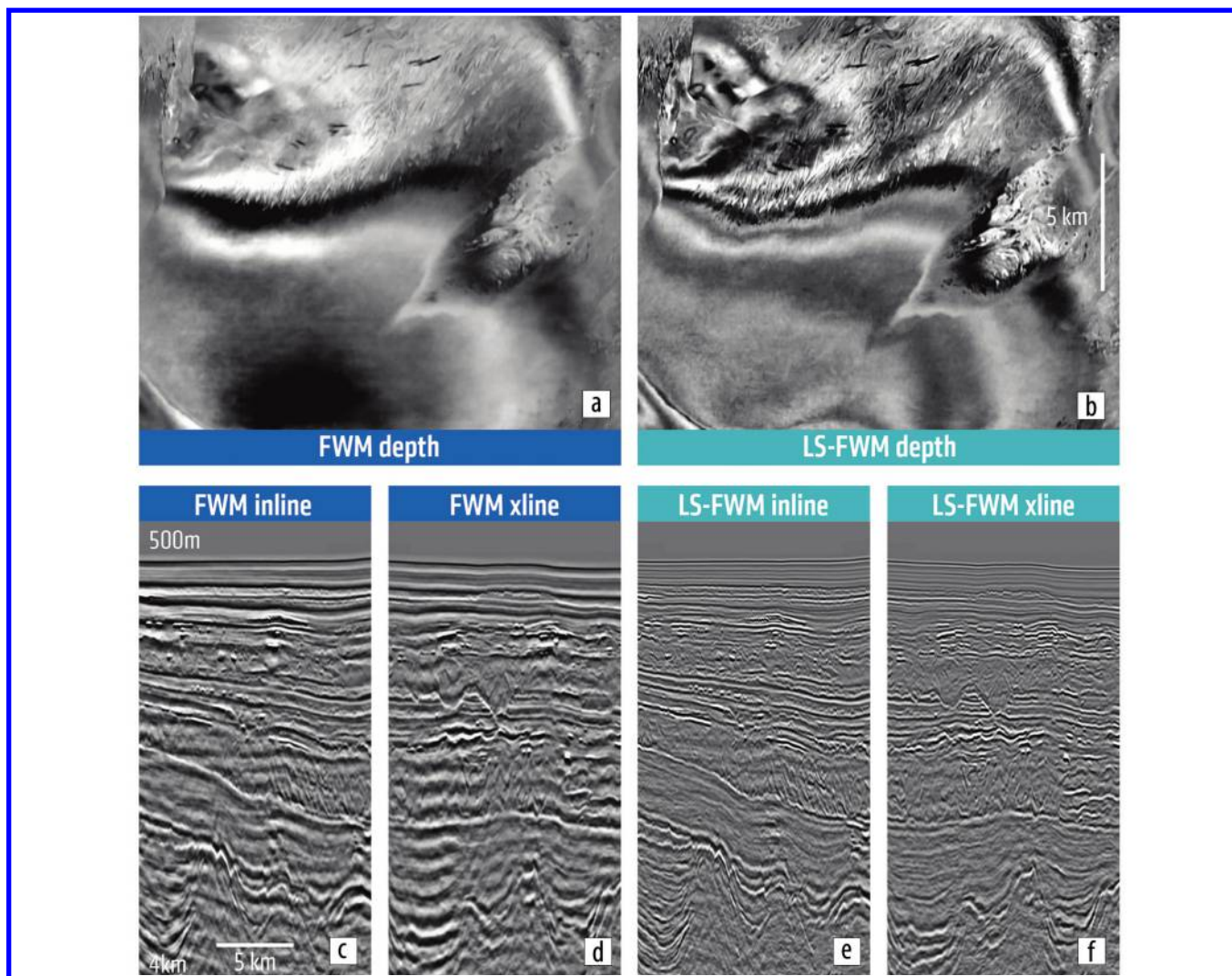


Figure 8. FWM versus LS-FWM with 3D WAZ data from the gulf: (a) FWM, depth = 1150 m; (b) LS-FWM, depth = 1150 m; (c) FWM inline; (d) FWM xline; (e) LS-FWM inline; and (f) LS-FWM xline.

(Korsmo et al., 2017). The standard migration images are severely contaminated by the acquisition footprint that is typical for shallow-water environments (Figure 6a). The LSM solution greatly reduces the acquisition footprint, resulting in a more interpretable shallow image (Figure 6e). LSM also creates images with broader wavenumber content (Figure 6f) compared to standard migration (Figure 6b). Fault planes are also better resolved using LSM solution (Figure 6h).

LS-FWM. The LS-FWM (Table 1) was applied to the 2D synthetic Sigsbee2b data in Figure 7. FWM crosstalk in Figure 7a (indicated by arrows) is successfully mitigated in the LS-FWM inversion result of Figure 7b. Moreover, LS-FWM enhances the imaging illumination and resolution by comparison to standard FWM.

The final LS-FWM results shown in Figure 8 use the 3D WAZ field data from the gulf as used in Figures 4 and 5. The major benefits of least-squares inversion are crosstalk rejection, illumination, and resolution enhancements. Furthermore, LS-FWM (Figure 8b) improves the imaging illumination by comparison to LSM of primaries only, in which the acquisition footprint is still evident (indicated by arrows in Figure 4).

Conclusions

We present an efficient and stable LSM that can be used for FWM of primaries and high-order reflected energy. Successful applications to both synthetic and field-data examples demonstrate its capability for broadband imaging. Results demonstrate that LS-FWM greatly improves the imaging illumination, mitigates acquisition footprint, reduces the crosstalk problem in SWIM and FWM, and produces a good estimate of the earth reflectivity. **ITE**

Acknowledgments

The authors would like to thank PGS for permission to publish this work and for the approval to show the MultiClient Gulf of Mexico data. We are also grateful to Aker BP for permission to publish the North Sea results. Furthermore, we thank Øystein Korsmo and Grunde Rønholdt for their support during the North Sea project, and our colleagues Xiang Li, Lingyun Qiu, and Cheng Cheng for their help at various stages of the project.

Corresponding author: shaoping.lu@pgs.com

References

Carlson, D., A. Long, W. Söllner, H. Tabti, R. Tenhamn, and N. Lunde, 2007, Increased resolution and penetration from a towed dual-sensor streamer: *First Break*, **25**, 71–77.
Cohen, J., F. Hagin, and N. Bleistein, 1986, Three-dimensional Born inversion with an arbitrary reference: *Geophysics*, **51**, no. 8, 1552–1558, <https://doi.org/10.1190/1.1442205>.

Goldstein, T., and S. Osher, 2009, The split Bregman method for L1-regularized problems: *SIAM Journal on Imaging Sciences*, **2**, no. 2, 323–343, <https://doi.org/10.1137/080725891>.
Korsmo, Ø., O. J. Askim, Ø. Runde, and G. Rønholdt, 2017, High fidelity velocity model building, imaging and reflectivity inversion — A case study over the Viking Graben area, Norwegian North Sea: 79th Conference and Exhibition, EAGE, Extended Abstracts, Tu A2 13, <https://doi.org/10.3997/2214-4609.201700818>.
Lailly, P., 1983, The seismic inverse problem as a sequence of before stack migrations: Conference on Inverse Scattering, Theory and Application, Society for Industrial and Applied Mathematics, Expanded Abstracts, 206–220.
Lu, S., D. Whitmore, A. Valenciano, and N. Chemingui, 2015, Separated-wavefield imaging using primary and multiple energy: *The Leading Edge*, **34**, no. 7, 770–778, <https://doi.org/10.1190/tle34070770.1>.
Lu, S., D. Whitmore, A. Valenciano, N. Chemingui, and G. Rønholdt, 2016, A practical crosstalk attenuation method for separated wavefield imaging: 86th Annual International Meeting, SEG, Expanded Abstracts, 4235–4239, <https://doi.org/10.1190/segam2016-13849878.1>.
Nemeth, T., C. Wu, and G. Schuster, 1999, Least-squares migration of incomplete reflection data: *Geophysics*, **64**, no. 1, 208–221, <https://doi.org/10.1190/1.1444517>.
Paige, C. C., and M. A. Saunders, 1982, LSQR: An algorithm for sparse linear equations and sparse least squares: *ACM Transactions on Mathematical Software*, **8**, no. 1, 43–71, <https://doi.org/10.1145/355984.355989>.
Prucha, M., and B. Biondi, 2002, Subsalt event regularization with steering filters: 72nd Annual International Meeting, SEG, Expanded Abstracts, 1176–1179, <https://doi.org/10.1190/1.1816859>.
Qiu, L., N. Chemingui, Z. Zou, and A. Valenciano, 2016, Full-waveform inversion with steerable variation regularization: 86th Annual International Meeting, SEG, Expanded Abstracts, 1174–1178, <https://doi.org/10.1190/segam2016-13872436.1>.
Rudin, L. I., S. Osher, and E. Fatemi, 1992, Nonlinear total variation based noise removal algorithms: *Physica D: Nonlinear Phenomena*, **60**, no. 1–4, 259–268, [https://doi.org/10.1016/0167-2789\(92\)90242-F](https://doi.org/10.1016/0167-2789(92)90242-F).
Schuster, G., 1993, Least-squares cross-well migration: 63rd Annual International Meeting, SEG, Expanded Abstracts, 110–113, <https://doi.org/10.1190/1.1822308>.
Strohmer, T., and R. Vershynin, 2009, Comments on the randomized Kaczmarz method: *The Journal of Fourier Analysis and Applications*, **15**, no. 4, 437–440, <https://doi.org/10.1007/s00041-009-9082-0>.
Tarantola, A., 1984, Inversion of seismic reflection data in the acoustic approximation: *Geophysics*, **49**, no. 8, 1259–1266, <https://doi.org/10.1190/1.1441754>.
Valenciano, A. A., B. Biondi, and A. Guitton, 2006, Target-oriented wave-equation inversion: *Geophysics*, **71**, no. 4, A35–A38, <https://doi.org/10.1190/1.2213359>.